

## Article

# Highly Stable Inverted Organic Solar Cell Structure Using Three Efficient Electron Transport Layers

Mohamed El Amine Boudia  and Cunlu Zhao 

MOE Key Laboratory of Thermo-Fluid Science and Engineering, School of Energy and Power Engineering, Xi'an Jiaotong University, Xi'an 710049, China; amineboudia@stu.xjtu.edu.cn

\* Correspondence: mclzhao@xjtu.edu.cn

**Abstract:** The efficiency of organic solar cells (OSCs) is influenced by various factors, among which environmental temperature plays a significant role. Previous studies have shown that the thermal stability of these cells can be enhanced by incorporating a third component into their structure. Ternary organic solar cells, particularly, have shown promising results in improving thermal stability. A well-designed electron transport layer (ETL) can significantly bolster thermal stability by facilitating efficient charge transport and reducing charge recombination. In this study, we investigated the effect of temperature, ranging from 300 K to 400 K, on the efficiency of inverted ternary structures by using a one-dimension optoelectronic model on “Oghma-Nano 8.0.034” software. The structures examined include (S1) “FTO/SnO<sub>2</sub>/PM6:D18:L8-BO/PEDOT: PSS/Ag”, (S2): “FTO/C<sub>60</sub>/PM6:D18:L8-BO/PEDOT: PSS/Ag”, and (S3): “FTO/PC<sub>60</sub>BM/PM6:D18:L8-BO/PEDOT: PSS/Ag”. Simulations using three different ETLs—SnO<sub>2</sub>, C<sub>60</sub>, and PC<sub>60</sub>BM—at 340 K (66.85 °C) resulted in a main effect on open circuit voltage ( $V_{oc}$ ) and fill factor ( $FF$ ) values, in addition to an important  $J_{sc}$  value in terms of thermally stable devices. However, these structures retained 92% of their initial ~20% efficiency observed at 300 K, demonstrating significant thermal stability under high power conversion efficiency ( $PCE$ ) conditions.

**Keywords:** organic solar cells; ternary structures; operating temperature; electron transport layer; power conversion efficiency



Academic Editors: Hengkai Zhang and Zhiliang Chen

Received: 12 December 2024

Revised: 30 December 2024

Accepted: 2 January 2025

Published: 3 January 2025

**Citation:** Boudia, M.E.A.; Zhao, C. Highly Stable Inverted Organic Solar Cell Structure Using Three Efficient Electron Transport Layers. *Energies* **2025**, *18*, 167. <https://doi.org/10.3390/en18010167>

**Copyright:** © 2025 by the authors. Licensee MDPI, Basel, Switzerland. This article is an open access article distributed under the terms and conditions of the Creative Commons Attribution (CC BY) license (<https://creativecommons.org/licenses/by/4.0/>).

## 1. Introduction

Currently, the international community faces a multifaceted global energy challenge, closely intertwined with the issue of global warming, primarily induced by greenhouse gasses, especially CO<sub>2</sub>, in the atmosphere [1–6]. Fossil fuels, as the principal sources of approximately 90% of CO<sub>2</sub> emissions and over 70% of all greenhouse gas emissions worldwide, are significant drivers of climate change [7–12]. These gasses trap solar heat, contributing to a rise in global temperatures [13–16].

Addressing global warming necessitates sustainable interventions, including reducing air pollution, which can be achieved through adopting renewable energy sources, minimizing waste, and conserving natural resources [13,17–19]. In this context, photovoltaic energy emerges as a sustainable and long-lasting solution that could mitigate the impacts of global warming [20–22]. OSCs, in particular, represent a promising alternative to traditional silicon-based panels due to their environmental benefits and cost efficiency in production [23]. Their widespread adoption could significantly enhance global solar energy utilization and reduce the ecological impacts of human activities [20]. Particularly, the role of OSCs in reducing global warming effects is increasingly recognized [23–25]. Although

their potential benefits are substantial, further research and development are critical to improve their efficiency and thermal stability [26–30].

The ETL is essential for determining the thermal stability of inverted ternary OSCs due to multiple factors [31]. An ETL that is well designed and has a consistent surface morphology can efficiently inhibit the penetration of moisture and prevent deterioration in high-humidity circumstances [31]. Effective engineering of the ETL can mitigate surface flaws, which have a negative impact on the performance and stability of the device.

Optimizing the ETL can improve the interfacial contact between the ETL and the organic active layer, leading to enhanced charge extraction and less recombination, hence enhancing thermal stability [32]. Modifying the ETL can drastically reduce the energy barrier at the ETL/organic contact, further increasing charge transmission and thermal stability [32].

Therefore, solution-processed ETLs, such as SnO<sub>2</sub> (Tin(IV)), have been studied for constructing high-performance inverted ternary OSCs with better thermal stability [33]. In addition, SnO<sub>2</sub> has an advantage in terms of high electron mobility of  $2 \times 10^{-9} \text{ m}^2 \text{ v}^{-1} \text{ s}^{-1}$  and a high glass transition temperature ( $T_g$ ) of 473–573 K, which suggests that this material can be an efficient ETL in OSC structures. Among efficient ETLs, we identify PC<sub>60</sub>BM ([6,6]-Phenyl-C61-butyric acid methyl ester) for aiding the extraction of electrons from the photoactive layer to the ETL and electrode. The high electron mobility of PC<sub>60</sub>BM, approximately  $2 \times 10^{-7} \text{ m}^2 \text{ v}^{-1} \text{ s}^{-1}$ , facilitates rapid electron movement, lowering the likelihood of recombination [34]. Furthermore, PC<sub>60</sub>BM has a high  $T_g$  of 430 K, which leads to it being considered among stable fullerene derivative structures and commonly used in OSCs. Additionally, it plays a critical function in determining the architecture of the photoactive layer, producing a bicontinuous network with the donor polymer for effective charge transport [34].

Employing C<sub>60</sub> (Buckminsterfullerene) as an ETL in inverted ternary OSCs has notable advantages, including its exceptional electron mobility, which enhances efficient charge mobility [35]. Utilizing C<sub>60</sub> in OSCs can decrease charge recombination rates, leading to more efficient charge extraction and higher *PCE*. Additionally, using C<sub>60</sub> as an ETL in OSCs improves device stability by reducing voltage hysteresis compared to traditional ETLs [35]. According to some previous studies, C<sub>60</sub> has a notably good performance in terms of *PCE* because it has a high electron mobility of  $1.2 \times 10^{-7} \text{ m}^2 \text{ v}^{-1} \text{ s}^{-1}$  and a  $T_g$  of over 400 K, which explain why it is advantageous in OSC structures. This stability is advantageous for maintaining long-term performance under operational circumstances, particularly in high-temperature environments [35,36]. ETLs based on C<sub>60</sub> can enhance the resilience of ternary OSCs against light-induced degradation. This enables OSCs to maintain their performance for longer durations, even when subjected to continuous illumination [35].

Improving the thermal stability of OSCs is vital for advancing their commercial viability and operational reliability. Ongoing research focuses on developing new materials and structures that optimize both *PCE* and thermal stability. Recent research by Zhang et al. [29] highlights the efficacy of the ternary blend approach in enhancing the thermal stability of OSCs, and it was found that the *PCE* of the device at 76.85 °C remained, on average, 80% of its *PCE* at room temperature. Key contributors to the charge-transfer state energy in these cells were identified as PBDB-T and IDT-PDOT-C6, with ITC6-2F playing a crucial role in facilitating charge carrier transfers to IDT-PDOT-C6. This mechanism promotes the generation of additional excitons reaching the donor/acceptor interface, thereby achieving high-efficiency photoelectric conversion [29]. Anass et al. [37] studied the influence of temperature on the performance of solar cells with [(Cbz-Mth)-B-T]2-PCBM as an active blend, and they found that their structure kept 89% of its room-temperature *PCE* at 76.85 °C. Another study conducted by Muhammad et al. [38] performed a simulation by stepping up the temperature from 300 K to 400 K to study the impact of raised temperatures on the efficiency of solar cells

with PBDB-T:ITIC-OE as the photoactive layer, and they obtained a loss ratio of efficiency in a temperature range of 300–350 K of approximately 9%, which indicates a highly stable device. Moreover, the use of charge transport layers is paramount in improving the *PCE* of OSCs. These layers are essential for the efficient extraction and mobility of charges, while also preventing electron leakage, and are utilized extensively across various materials in inverted OSC architectures [39–43]. Previous studies conducted by Anass et al. [37] and Muhammad et al. [38] found that the best thermal stability achieved by OSCs at 350 K is 9%, but the *PCEs* achieved in these studies were 7.4% and 6.2%, respectively, which is relatively low. It is challenging to achieve high thermal stability and high *PCE* at the same time.

This study aims to explore how temperature variations affect the efficiency of inverted bulk heterojunction (BHJ) OSCs. Temperature variation significantly affects the efficiency of inverted bulk heterojunction OSCs through several mechanisms: as increased temperatures can enhance charge carrier mobility in inverted BHJ OSCs, they also lead to increased recombination rates, reduced  $V_{oc}$ , and potential material degradation. Understanding and optimizing these factors is essential for improving the thermal stability and efficiency of OSCs, especially for applications in diverse environmental conditions. Through simulations using three different electron transport layers— $\text{SnO}_2$ ,  $\text{C}_{60}$ , and  $\text{PC}_{60}\text{BM}$ —we seek to derive insights into the performance and thermal stability of these OSCs, specifically focusing on analyses of their high thermal stability (quantified by the *PCE* loss ratio) at 350 K under a high *PCE* of ~20%. This could potentially lead to the development of more efficient and stable OSCs in laboratory settings.

For the reader's knowledge, these are purely original structure models with a device area of  $4.84 \text{ mm}^2$  that were designed and performed inspired by a previous study conducted by Zhu et al. [44]. Furthermore, we selected the ETLs  $\text{SnO}_2$ ,  $\text{C}_{60}$ , and  $\text{PC}_{60}\text{BM}$  because of the benefits shown in other studies, as we mentioned previously in the Introduction section as well as Table 1, and due to their high electron mobilities of  $2 \times 10^{-9} \text{ m}^2 \text{ v}^{-1} \text{ s}^{-1}$ ,  $1.2 \times 10^{-7} \text{ m}^2 \text{ v}^{-1} \text{ s}^{-1}$ , and  $2 \times 10^{-7} \text{ m}^2 \text{ v}^{-1} \text{ s}^{-1}$ , respectively; additionally, as shown in Table 1, these selected ETLs have a high  $T_g$  of 473–573 K, 393–403 K, and 430 K, respectively. The simulated device structures are mentioned in Figure 1.

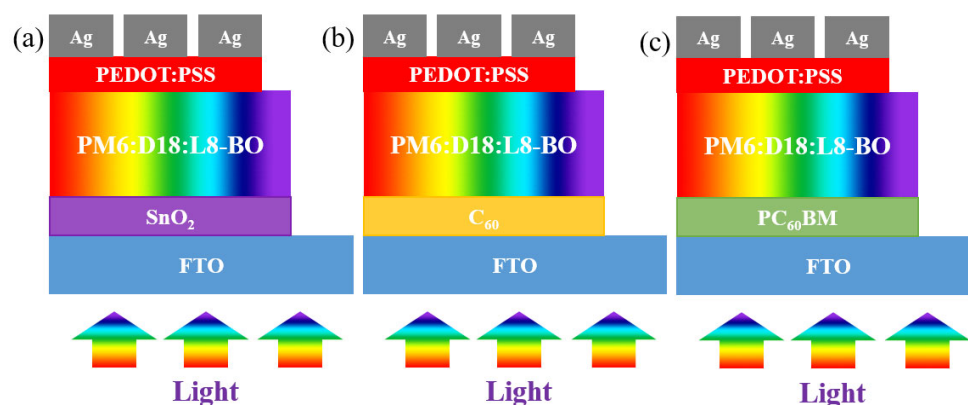


**Figure 1.** Schematic illustration of the structures under light exposure: (a) S1 under light exposure with a device area of  $4.84 \text{ mm}^2$ ; (b) S2 under light exposure with a device area of  $4.84 \text{ mm}^2$ ; (c) S3 under light exposure with a device area of  $4.84 \text{ mm}^2$ .

**Table 1.** The  $T_g$  and electron motilities of the ETLs.

Materials	$T_g$ (K)	Electron Mobility ( $\text{m}^2 \text{ v}^{-1} \text{ s}^{-1}$ )
$\text{SnO}_2$	473–573	$2 \times 10^{-9}$
$\text{C}_{60}$	393–403	$1.2 \times 10^{-7}$
$\text{PC}_{60}\text{BM}$	430	$2 \times 10^{-7}$

## 2. The Simulation Model and Performance Indicators

The simulation employs Oghma-Nano software, which utilizes a one-dimensional drift diffusion model under standard conditions (with a temperature variation within the range of 300–400 K) for its electrical modeling. The model includes the solution of bi-polar drift diffusion, charge carrier continuity, Poisson equation, and Maxwell–Boltzmann equation free charge carrier statistics. The mathematical model can be found in the software’s documentation for more detailed information [45].

The position variable in the simulation of OSCs utilizing one-dimensional models, such as Oghma-Nano, is integral to understanding the performance attributes of these solar cells. This variable facilitates the modification of layer thicknesses within the OSC architecture. Alterations in the thickness of the active layer can markedly affect charge generation and transport, thereby influencing key parameters such as  $J_{sc}$  and  $V_{oc}$ . Furthermore, the position variable is instrumental in modeling the electric field across the various layers of the solar cell. A uniformly distributed electric field is vital for efficient charge separation and collection, which in turn directly affects the overall efficiency of the device, as determined by the Poisson equation within the simulation framework. By simulating various positions for charge carriers, including electrons and holes, researchers can evaluate the efficacy of carrier movement throughout the device. This analysis examines recombination rates and the thermal effects on electrons and holes, essential for enhancing device performance. Additionally, simulations can account for temperature variations across different positions within the solar cell, enabling an evaluation of how thermal influences affect performance metrics such as  $FF$  and  $PCE$  under realistic operating conditions. The simulated structure of the device is FTO/ETL/PM6:D18:L8-BO (Poly[(2,5-bis(2-ethylhexyl)-1,3,4-oxadiazole-2,5-diyl)-alt-(3-hexylthiophene-2,5-diyl)]:4,4'-(2,5-bis(2-ethylhexyl)-1,3,4-oxadiazole-2,5-diyl)bis(3-hexylthiophene):2,2'-((2,5-bis(2-ethylhexyl)-1,3,4-oxadiazole-2,5-diyl)bis(3-hexylthiophene)) bis(benzo[1,2-b:4,5-b']dithiophene))/PEDOT: PSS (Poly(3,4-ethylenedioxythiophene) polystyrene sulfonate)/Ag (Silver), and the input parameters and thicknesses are included in Tables 1 and 2. The input electrical parameters include the average mobilities, the effective densities of free electrons and holes per position  $x$ , recombination rates, and other important parameters in the drift diffusion model and the charge carrier continuity equations to determine the J-V characteristics and other measurement outputs. In addition, the energy bandgap is considered 1.29 eV for the active blend PM6:D18:L8-BO (0.8:0.2:1.2). All these values’ details are included in Tables 2 and 3.

**Table 2.** Simulation parameters of Oghma-nano software.

Parameters	Values	Ref.
Electron mobility ( $\mu_e$ )	$1.49 \times 10^{-7} \text{ m}^{-2}\text{V}^{-1}\text{s}^{-1}$	[44]
Hole mobility ( $\mu_h$ )	$1.42 \times 10^{-7} \text{ m}^{-2}\text{V}^{-1}\text{s}^{-1}$	[44]
Effective density of free electron ( $N_c$ at 300 K)	$1 \times 10^{26} \text{ m}^{-3}$	[44]
Effective density of free hole ( $N_v$ at 300 K)	$1 \times 10^{26} \text{ m}^{-3}$	[44]
$n$ to $P$ recombination rate constant	$1.15 \times 10^{-17} \text{ m}^{-3}\text{s}^{-1}$	[44]
Free electron ( $n$ ) to trapped electron ( $strap$ )	$1 \times 10^{-15} \text{ m}^{-2}$	[44]
Trapped electron ( $n_{trap}$ ) to free hole ( $P$ )	$1 \times 10^{-20} \text{ m}^{-2}$	[44]
Trapped hole ( $P_{trap}$ ) to free electron ( $n$ )	$1 \times 10^{-20} \text{ m}^{-2}$	[44]
Free hole ( $P$ ) to trapped hole ( $P_{trap}$ )	$1 \times 10^{-15} \text{ m}^{-2}$	[44]
Number of traps ( $N_t$ )	5 Traps	[44]

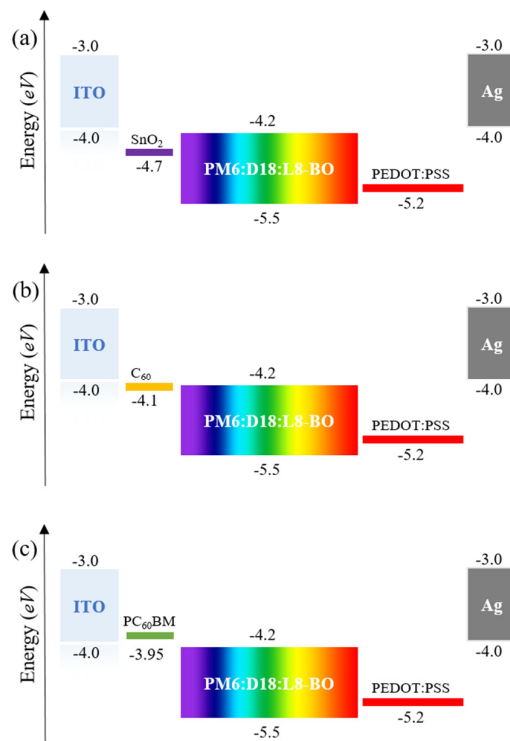
**Table 2.** *Cont.*

Parameters	Values	Ref.
Energy bandgap ( $E_g$ )	1.29 eV	[44]
Relative permittivity ( $\epsilon_r$ )	3.0 a.u	[44]

**Table 3.** The thicknesses of the materials used in the three structures.

Layer	Thickness (nm)	Materials	Type
ITO	130	Oxides	Contact
SnO <sub>2</sub>	5	Oxides	ETL
C <sub>60</sub>	5	Small molecules	ETL
PC <sub>60</sub> BM	5	Polymers	ETL
PM6:D18:L8-BO (0.8:0.2:1.2)	80	Blends	Active
PEDOT: PSS	20	Polymers	HTL
Ag	100	Metal	Contact

Figure 2a–c represent the energy levels of OSC structures S1, S2, and S3, respectively. All the ETLs in the different structures show cascaded energy levels in terms of the lowest unoccupied molecular orbital (*LUMO*) between the active layer of  $-4.2$  eV and SnO<sub>2</sub>, C<sub>60</sub>, and PC<sub>60</sub>BM, which are  $-4.7$  eV,  $-4.1$  eV, and  $-3.95$  eV, respectively. The cascaded energy levels create more straightforward pathways in terms of electron and hole transport. PEDOT:PSS forms a close energy level in terms of the highest occupied molecular orbital (*HOMO*), with an active layer of  $-5.5$  eV. An efficient electron transport further affects the  $V_{oc}$  and  $FF$  values as analyzed later in Section 3.

**Figure 2.** The energy levels of the materials used in the structures: (a) energy levels of S1; (b) energy levels of S2; (c) energy levels of S3.

The transfer of charges is determined by solving the drift diffusion equations that account for the movement of both electrons and holes. Bi-polar drift diffusion equations at position  $x$  for both electrons and holes are represented by Equations (1) and (2),

$$J_n = q\mu_e n_f \frac{\varphi}{\partial x} + qD_n \frac{\partial n}{\partial x} \quad (1)$$

$$J_p = q\mu_h p_f \frac{\partial \varphi}{\partial x} + qD_p \frac{\partial p}{\partial x} \quad (2)$$

where  $J_{n,p}$  is the electron and hole current density,  $q$  is the elementary charge,  $\mu_e$ , and  $\mu_h$  are the mobilities of electrons and holes, respectively;  $D_n$  and  $D_p$  are the electron and hole diffusion coefficients, respectively;  $n$  is the density of electrons, and  $p$  is the density of holes. The conservation of the charge carriers is ensured by resolving the continuity of charge carrier equations as specified in Equations (3) and (4). The charge carrier continuity equations are shown in Equations (3) and (4),

$$\frac{\partial J_n}{\partial x} = q(R_n - G + \frac{\partial n}{\partial t}) \quad (3)$$

$$\frac{\partial J_p}{\partial x} = -q(R_p - G + \frac{\partial p}{\partial t}) \quad (4)$$

where  $R_n$  and  $R_p$  are the recombination rates of electrons and holes, respectively;  $G$  is the generation rate.

The solution to Poisson's equation is used to determine the distribution of potential within the device, and it is represented as follows in Equation (5):

$$\frac{\partial \epsilon_0 \epsilon_r}{\partial x} \frac{\partial \varphi}{\partial x} = q(n - p) \quad (5)$$

where  $\epsilon_0$ ,  $\epsilon_r$ , the constants of permittivity in free space and relative permittivity, respectively, are constant;  $\varphi$  is the voltage profile. The model applies Maxwell-Boltzmann statistics to solve free carrier statistics as shown in Equations (6) and (7):

$$n = N_c \exp\left(\frac{F_n - E_c}{K_B T}\right) \quad (6)$$

$$p = N_v \exp\left(\frac{E_v - F_p}{K_B T}\right) \quad (7)$$

where  $N_c$ ,  $N_v$  are the constants of the effective density of states in the conduction and valence band of the semiconductor;  $F_{n,p}$  are constants of the energy level of the Fermi level in the valence and conduction band of the semiconductor;  $E_c$  is the conduction band,  $E_v$  is the valence band,  $K_B$  is the Boltzmann constant, and  $T$  is the temperature.

The boundary conditions between the layer interfaces are represented as the tunneling of electrons and holes through layer interfaces provided by Equations (8) and (9):

$$J_n = -qT_e \left[ (n_1 - n_1^{eq}) - (n_0 - n_0^{eq}) \right] \quad (8)$$

$$J_p = -qT_h \left[ (p_1 - p_1^{eq}) - (p_0 - p_0^{eq}) \right] \quad (9)$$

where  $T_e$  and  $T_h$  are the rate constants of tunneling of electrons and holes, respectively;  $n_{0,1}$  is the number of electrons in the layers before and after the interface;  $p_{0,1}$  is the number of holes before and after the interface;  $n_{0,1}^{eq}$  is the equilibrium number of electrons in before and after the interface;  $p_{0,1}^{eq}$  is the equilibrium number of holes in the layers before and after the interface.

More details of the above electrical model of our simulation can be found in Refs. [46–48].

OSC performance is commonly measured by several key metrics that directly influence their efficiency and thermal stability. These indicators are detailed below.

PCE is the ratio of the electrical output of the solar cell to the incident light energy.

$$PCE = \frac{P_{max}}{I_{in}} = \frac{J_{sc}V_{oc}FF}{I_{in}} \quad (10)$$

where  $P_{max}$  is the maximum power output by the OSC and  $I_{in}$  is the illumination intensity. The  $V_{oc}$  value represents the highest voltage when the current through the device is null, and it is represented as follows in Equation (11):

$$V_{oc} = \frac{E_g - \Delta E}{q} \quad (11)$$

where  $\Delta E$  is the energy offset.

The generation of charge and the overall performance of OSCs are significantly influenced by the energy offset. This indicates the discrepancy in energy levels between the acceptor material's lowest unoccupied molecular orbital (LUMO) and the donor material's highest occupied molecular orbital (HOMO), as represented in Equations (12) and (13):

$$qV_{oc} = E_g - \Delta E \quad (12)$$

$$\Delta E = 2\left(E_{F,h} - E_{HOMO}^D\right) - K_B T \ln\left(\frac{e}{h}\right) \quad (13)$$

where  $\Delta E$  is the energy offset;  $E_{F,h}$  is the energy corresponding fermi-level;  $E_{HOMO}^D$  is the electron donor energy.  $FF$  represents the maximum power output of the OSC, which is defined below in Equation (14):

$$FF = \frac{P_{max}}{V_{oc}J_{sc}} = \frac{V_m}{V_{oc}} \left[1 - e^{-\frac{q}{AKT}(V_m - V_{oc})}\right] \quad (14)$$

where  $P_{max}$  is the maximum power delivered by the OSC,  $V_m$  is the maximum voltage, and  $A$  is the ideality factor of the semiconductor. Equation 15 describes the current–voltage (J-V) characteristics of OSCs.

$$J(V) = J_0 \left[ \exp\left(\frac{eV}{AKT}\right) - 1 \right] + J_{ph} \quad (15)$$

where  $J_0$  is the reverse saturation current density,  $e$  is the charge of an electron, and  $J_{ph}$  is the photo-current density.

### 3. Results and Discussion

The density of  $J$ - $V$  was simulated under AM 1.5 G illumination with an intensity of  $100 \text{ mW cm}^{-2}$  and a temperature range between 300 K and 400 K. S1 showed the best PCE of 20.08% at 300 K with a  $J_{sc}$  of  $27.4 \text{ mA cm}^{-2}$ , a  $V_{oc}$  of 0.89 V, and an  $FF$  of 82.2%, while the performance relatively decreased between the range of 310 and 400 K to reach a PCE of 15.53%, a  $J_{sc}$  of  $27.35 \text{ mA cm}^{-2}$ , a  $V_{oc}$  of 0.73 V, and an  $FF$  of 77.7% at 400 K. As mentioned, the major parameters that cause a reduction in the efficiency of OSCs during the enhancement of temperature are  $V_{oc}$  and  $FF$  (see Figures 3a and 4b,c).

The increase in temperature causes an augmentation of energy loss ( $\Delta E$ ) as demonstrated by Equation (13), and then  $V_{oc}$  decreases as a result of that augmentation.  $FF$  showed a negative correlation with temperature, which decreased when the temperature increased from 300 K to 400 K (from  $26.85 \text{ }^\circ\text{C}$  to  $126.85 \text{ }^\circ\text{C}$ ). The performance decrease of  $FF$  was due

to the increase in the exponential of the temperature, as demonstrated in Equation (14).  $J_{sc}$  showed a relative stability under the increase in temperature. The reduction in  $J_{sc}$  can be attributed to the bandgap energy ( $E_g$ ) effect. As temperature rises,  $J_{sc}$  experiences a marginal increase due to the reduction in  $E_g$ . Consequently, a greater number of photons possess adequate energy to generate electron–hole pairs. Nevertheless, the impact of this phenomenon is quite minor. The exponential relationship between temperature and the reverse saturation current of photovoltaic cells is observed in Equation (15). Additionally, this factor can have an impact on  $J_{sc}$ .

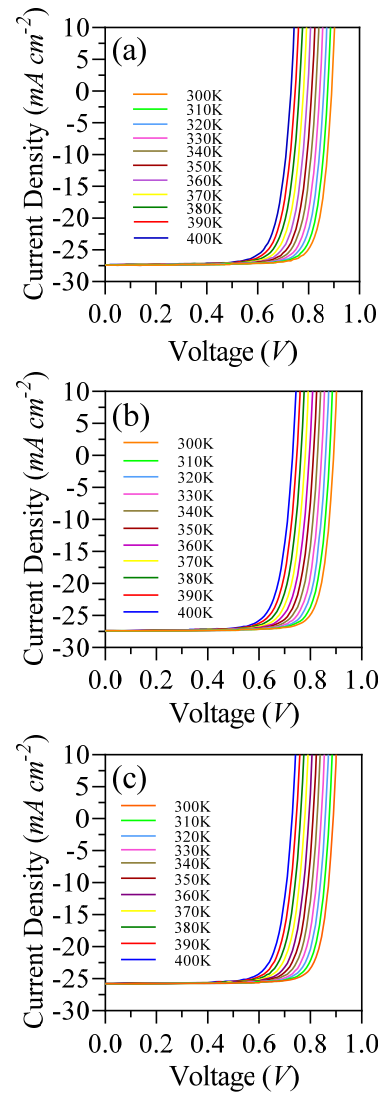


**Figure 3.** (a)  $J$ - $V$  curves of the S1 device in a temperature range of 300–400 K for a device area of  $4.84 \text{ mm}^2$ ; (b)  $J$ - $V$  curves of the S2 device; (c)  $J$ - $V$  curves of S3 device.

The second structure's results are presented in Figures 3b and 4. S2 showed the best  $PCE$  of 19.88% at 300 K with a  $J_{sc}$  of  $27.15 \text{ mA cm}^{-2}$ , a  $V_{oc}$  of 0.89 V, and an  $FF$  of 82.3%, while the efficiency relatively decreased in the range between 310 and 400 K to reach a  $PCE$  of 15.25%, a  $J_{sc}$  of  $26.78 \text{ mA cm}^{-2}$ , a  $V_{oc}$  of 0.73 V, and an  $FF$  of 78% at 400 K. These results for behave similarly to those for S1 and are slightly decreased in comparison. As depicted by the results for S2, the major parameters that cause a decrease in the performance of this device during the enhancement of temperature are fundamentally the same as before  $V_{oc}$  and  $FF$  (see Figure 4b,c).

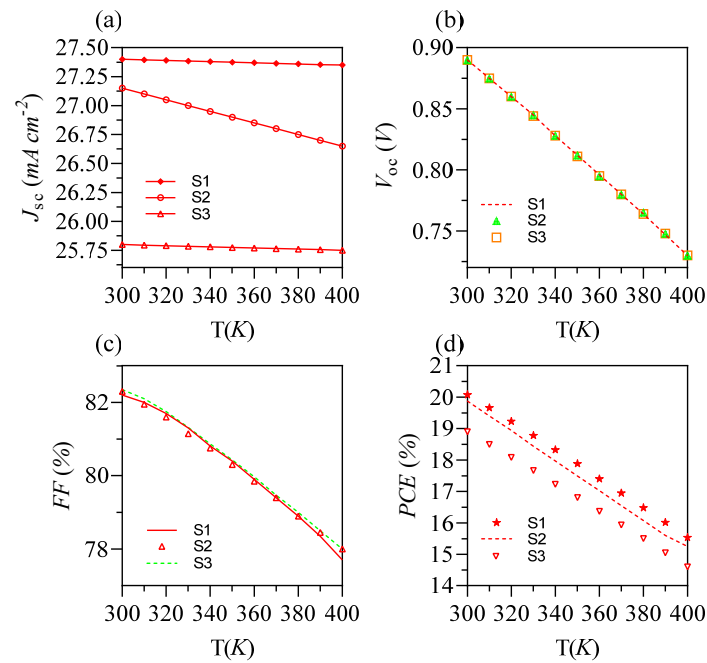


**Figure 4.** Temperature effects on the performance of the S1, S2, and S3 devices: (a)  $J_{sc}$  as a function of temperature; (b)  $V_{oc}$  as a function of temperature; (c) FF as a function of temperature; and (d) PCE as a function of temperature.

The increase in temperature caused an enhancement of  $\Delta E$  as demonstrated by Equation (13), and then  $V_{oc}$  decreased because of that enhancement. The diminution in  $J_{sc}$  can be attributed to the concept of  $E_g$ . As temperature rises, the short-circuit current,  $J_{sc}$ , experiences a slight increase due to the reduction in  $E_g$ . This decrease in bandgap energy enables a greater number of photons to possess sufficient energy for the generation of excitons. The reverse saturation current of photovoltaic cells exhibits an exponential growth pattern about temperature. Additionally, this factor can have an impact on the magnitude of  $J_{sc}$ , as demonstrated in Equation (15).

The third structure is presented in Figure 1, and its outcomes are depicted in Figures 3c and 4. At a temperature of 300 K, S3 exhibited the highest PCE of 18.9%. This was accompanied by a  $J_{sc}$  of 25.8 mA cm<sup>-2</sup>, a  $V_{oc}$  of 0.89 V, and an FF of 82.36%. However, when the temperature increased to a range from 310 to 400 K, the performance of S3 declined.

At 400 K, PCE reduced to 14.6%, with a  $J_{sc}$  of 25.76 mA cm<sup>-2</sup>, a  $V_{oc}$  of 0.73 V, and an FF of 78%. According to the findings from the results for S3, it can be observed that the primary factors contributing to the decline in the device's performance as temperature increases remain consistent with  $V_{oc}$  and FF (refer to Figures 3c and 4b,c).

The rise in temperature leads to an increase in  $\Delta E$ , as indicated by Equations (12) and (13). Consequently,  $V_{oc}$  decreases as a result of this increase. The decrease in  $J_{sc}$  can be ascribed to  $E_g$ .  $J_{sc}$  undergoes a marginal augmentation as the temperature increases, primarily as a result of the decrease in  $E_g$ . The reduction in bandgap energy facilitates an increased likelihood of photons possessing the necessary energy to produce electron–hole pairs. The temperature-dependent behavior of photovoltaic cells' reverse saturation current is characterized by an exponential increase, as noted before in S1 and S2. Moreover, this particular element can influence the amount of  $J_{sc}$ , as exemplified in Equation (13).

The relationships between recombination, hole, and electron heating are essential to comprehending the effectiveness and performance of OSCs. When semiconductor materials absorb photons, the energy of the electrons increases, a phenomenon known as electron heating. This process is essential to OSCs because it produces electron–hole pairs when light is absorbed. Elevating electrons from the valence band to the conduction band with

the energy of absorbed photons results in an increase in kinetic energy. Similarly, the energy dynamics of holes are involved in whole heating. The hole left by an electron moving to the conduction band may also acquire energy from thermal processes or interactions with other charge carriers. Charge carrier dynamics can be greatly impacted by the solar cell's overall temperature, which is influenced by both electron and hole heating. Recombination heating occurs when electrons and holes recombine, releasing energy in the form of heat instead of contributing to electrical current.

We investigated the electron, hole, and recombination heating for S1, S2, and S3 OSCs to discover the influence of temperature on carrier dynamics and the impact of carrier dynamics on the performance indicators  $J_{sc}$ ,  $V_{oc}$ , and  $FF$ , which affect the  $PCE$  and the thermal stability of the devices. The investigation results of the carrier dynamics are depicted in Figures 5 and 6. Figure 5a,c,e represent the electron heating of S1, S2, and S3, respectively. Furthermore, Figure 5b,d,f represent the hole heating in S1, S2, and S3, respectively. We noticed peak values of charge carrier (electron and hole) heating in the position of 150 nm and saw increased electron heating values within the temperature range of 300–400 K. At 300 K, the devices showed peak values of  $2.78 \times 10^{11} \text{ J S}^{-1} \text{ m}^{-1}$ ,  $2.75 \times 10^{11} \text{ J S}^{-1} \text{ m}^{-1}$ , and  $2.3 \times 10^{11} \text{ J S}^{-1} \text{ m}^{-1}$  for S1, S1, and S3, respectively. Furthermore, at 400 K, the devices showed  $1.04 \times 10^{12} \text{ J S}^{-1} \text{ m}^{-1}$ ,  $1.05 \times 10^{12} \text{ J S}^{-1} \text{ m}^{-1}$ , and  $9.28 \times 10^{11} \text{ J S}^{-1} \text{ m}^{-1}$  for S1, S2, and S3, respectively. At the same position, the devices showed increased hole heating values within the temperature range of 300–400 K; at 300 K, the devices showed peak values of  $2.57 \times 10^{11} \text{ J S}^{-1} \text{ m}^{-1}$ ,  $2.63 \times 10^{11} \text{ J S}^{-1} \text{ m}^{-1}$ , and  $2.22 \times 10^{11} \text{ J S}^{-1} \text{ m}^{-1}$  for S1, S2, and S3, respectively, while at 400 K, the results were  $9.84 \times 10^{11} \text{ J S}^{-1} \text{ m}^{-1}$ ,  $9.86 \times 10^{11} \text{ J S}^{-1} \text{ m}^{-1}$ , and  $8.74 \times 10^{11} \text{ J S}^{-1} \text{ m}^{-1}$  for S1, S2, and S3, respectively.

The charge carrier dynamic was impacted by the increasing temperature in the three devices by increasing the interactions with other charge carriers. On the other hand, the recombination rates usually rise as temperatures rise as a result of electron and hole heating. The Arrhenius equation governs this, as shown in Equation (16), and it demonstrates how higher temperatures can speed up reaction rates, including recombination processes, as depicted in Figure 6.

$$k = Ae^{-\frac{E_a}{RT}} \quad (16)$$

where  $k$  is the rate constant of the reaction,  $A$  is the pre-exponential factor (indicating the frequency of collisions),  $E_a$  is the activation energy required for the reaction, and  $R$  is the universal gas constant (approximately 8.314 J mol K).

The recombination rate of S1, S2, and S3, as shown in Figure 6a, Figure 6b, and Figure 6c, respectively, is influenced by the increasing heating process of electrons and holes. While increasing the temperature, we noticed, as shown in Figure 6, that the recombination rate increased proportionally within the range of temperature of 300–400 K for all devices; at the same time, we noticed an inverse proportion of  $FF$  and  $V_{oc}$  specifically, as depicted in Figure 4b,c for S1, S2, and S3.

The materials used for the buffer and active layers have an impact on the production and movement of electrons. The heating profile is influenced by the energy levels and mobilities of various materials. The characteristics of the ETL can influence heating by either promoting or impeding electron mobility. By comparing the carrier dynamic results of electron, holes, and recombination heating rates between the devices using  $\text{SnO}_2$ ,  $\text{C}_{60}$ , and  $\text{PC}_{60}\text{BM}$ , we found that  $\text{PC}_{60}\text{BM}$  had slightly less recombination and charge carrier heating values in the increasing temperature range between 300 and 400 K, which explains the high  $FF$  and  $V_{oc}$  achieved by the device that used  $\text{PC}_{60}\text{BM}$  as an ETL. However, the devices using  $\text{SnO}_2$  and  $\text{C}_{60}$  as ETLs achieved approximately close values in terms of carrier heating dynamics and performance indicator parameters such as  $J_{sc}$ ,  $V_{oc}$ , and  $FF$ . At the

same time, they had a higher value of  $J_{sc}$  than the PC<sub>60</sub>BM device and higher PCE values in the entire range of 300–400 K as a result. Despite the stability of the PC<sub>60</sub>BM device in terms of  $FF$  and  $V_{oc}$ , the lower  $J_{sc}$  values achieved by this device can be attributed to its material properties, such as light absorption and less interaction with other charge carriers, which slightly decreases charge mobility, which affects the  $J_{sc}$  value as a result.

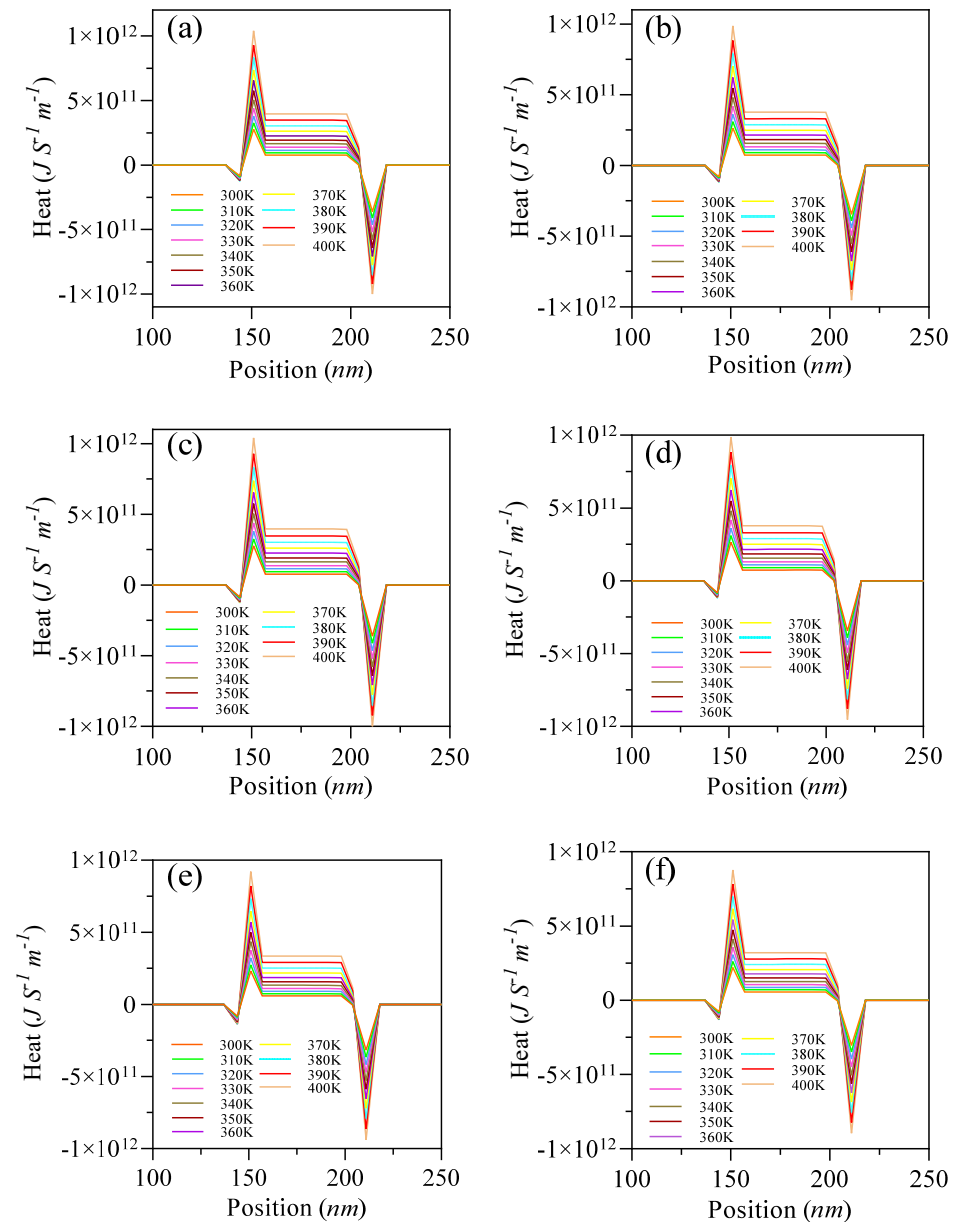


**Figure 5.** (a) Electron heating of S1 for temperature range of 300–400 K; (b) hole heating of S1 device; (c) electron heating of S2; (d) hole heating of S2; (e) electron heating of S3; (f) hole heating of S3.

We observed that all the structures—S1, S2, and S3—showed good performance in the temperature range between 300 and 340 K (from 26.85 °C to 66.85 °C) (see Table 4), which losses of only 8.7%, 9.6%, 8.8%, respectively, from their initial efficiency. The performance parameters  $J_{sc}$ ,  $V_{oc}$ , and  $FF$  had somewhat the same progression, while S3 achieved a lower PCE of 18.9% in comparison to S1 and S2, which achieved 20.08% and 19.88%, respectively. The inverted structure employing SnO<sub>2</sub> and C<sub>60</sub> achieved the best PCE of 20.08% and 19.88%, respectively; on the other hand, the inverted structure using PC<sub>60</sub>BM as an ETL showed a lower PCE. Nevertheless, all devices worked efficiently in terms of performance.

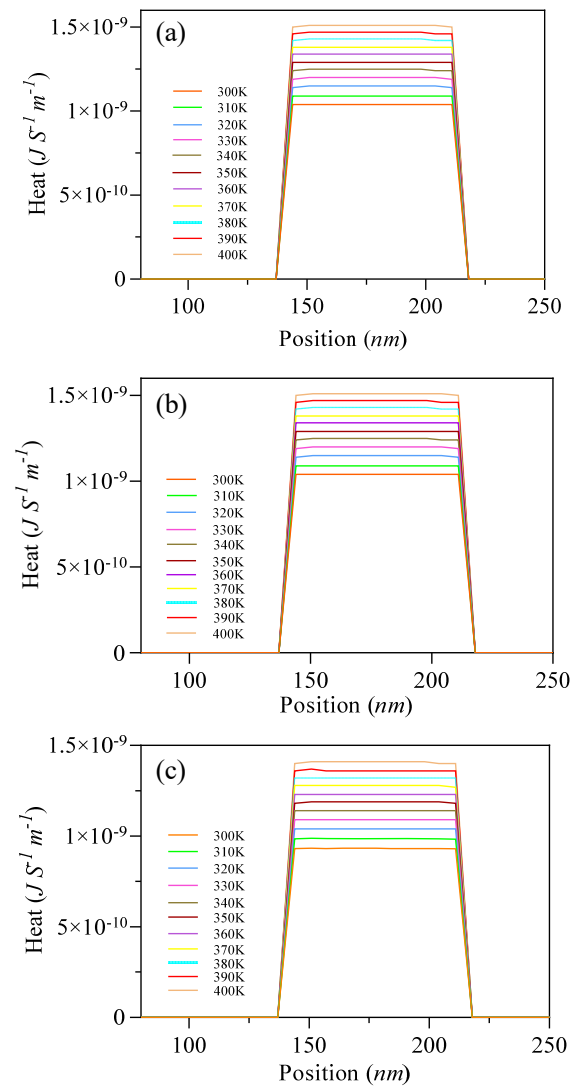


**Figure 6.** (a) Recombination heating of S1 for temperature range of 300–400 K; (b) recombination heating of S2; (c) recombination heating of S3.

**Table 4.** The photovoltaic parameters of three devices (S1, S2, and S3) under different temperatures.

	$T$ (K)	$T$ ( $^{\circ}$ C)	$J_{sc}$ ( $\text{mA cm}^{-2}$ )	$V_{oc}$ (V)	$FF$ (%)	$PCE$ (%)
S1	300	26.85	27.4	0.89	82.2	20.08
	310	36.85	27.4	0.875	81.97	19.66
	320	46.85	27.4	0.86	81.63	19.23
	330	56.85	27.4	0.84	81.26	18.78
	340	66.85	27.38	0.828	80.82	18.33
	350	76.85	27.38	0.812	80.4	17.88
	360	86.85	27.37	0.796	79.91	17.4
	370	96.85	27.37	0.78	79.38	16.95
	380	106.85	27.36	0.76	78.9	16.48
	390	116.85	27.36	0.747	78.35	16.01
	400	126.85	27.35	0.73	77.7	15.53

**Table 4.** *Cont.*

	<i>T</i> (K)	<i>T</i> (°C)	<i>J</i> <sub>sc</sub> (mA cm <sup>-2</sup> )	<i>V</i> <sub>oc</sub> (V)	<i>FF</i> (%)	<i>PCE</i> (%)
S2	300	26.85	27.15	0.89	82.3	19.88
	310	36.85	27.05	0.875	82	19.40
	320	46.85	27.05	0.86	81.6	18.94
	330	56.85	27.03	0.84	81.2	18.44
	340	66.85	26.80	0.83	80.8	17.97
	350	76.85	26.85	0.81	80.4	17.49
	360	86.85	26.65	0.8	79.9	17.03
	370	96.85	26.67	0.78	79.4	16.55
	380	106.85	26.80	0.76	78.9	16.07
	390	116.85	26.57	0.75	78.3	15.60
	400	126.85	26.78	0.73	78	15.25
S3	300	26.85	25.8	0.89	82.36	18.9
	310	36.85	25.8	0.87	82	18.5
	320	46.85	25.8	0.86	81.7	18.08
	330	56.85	25.79	0.84	81.32	17.67
	340	66.85	25.79	0.83	80.87	17.23
	350	76.85	25.78	0.81	80.43	16.81
	360	86.85	25.78	0.79	79.97	16.37
	370	96.85	25.77	0.78	79.43	15.93
	380	106.85	25.77	0.76	79	15.5
	390	116.85	25.77	0.75	78.4	15.05
	400	126.85	25.76	0.73	78	14.6

All the studies showed a stable loss ratio of around 11% between 300 K and 350 K according to the results shown in Table 4.

We investigated our results of the loss ratio of *PCE* as a function of increasing temperature with some other numerical studies, as shown in Table 5. The current study demonstrated the thermal stability of the devices, with a loss ratio of 11% at temperatures from 300 K to 350 K, in contrast to the results of Khan et al. and Kim et al., whose studies reported loss ratios of 15% and 17%, respectively.

**Table 5.** Results of the *PCE* loss ratio (%) due to temperature increment.

	<i>PCE</i> at 300 K	<i>PCE</i> at 350 K	Loss Ratio %
Khan et al. [49]	5.75%	4.88%	15%
Anass et al. [37]	8%	7.4%	9%
Muhammad et al. [38]	6.82%	6.2%	9%
Kim et al. [25]	3.25%	2.7%	17%
Our study	20.08%	17.88%	10.9%

Khan et al. performed a one-dimensional numerical simulation of a p-i-n OSC with a structure consisting of ITO/PEDOT: PSS/poly{4,4'-bis(2-ethylhexyl) dithieno [3,2-b:2',3'-d] silole-alt-5,6-difluoro-4,7-bis (4-hexylthiophen-2-yl)-2,1,3-benzothiadiazle}: [6,6]-phenyl-C61 butyric acid methyl ester (PDTSDTFFBT: PCBM/PCBM)/Ca/Al with an

emphasis on enhancing the PCE. They measured the effect of the temperature of the device within a range of 300–400 K. Kim et al. investigated OSC performance at a high operating temperature near 300–420 K by using a P-i-n OSC within the structure of ITO/PEDOT: PSS/P3HT: PCBM (1:0.8)/LiF/Al, with an emphasis on studying operating temperature stability, and they measured the effect of the temperature of a device using PEDOT: PSS as the HTL within a range of 300–450 K.

Muhammad et al. performed a one-dimensional numerical simulation of a n-i-p OSC with a structure consisting of FTO/PDINO(Perylene diimide N-oxide)/PBDB-T: ITIC-OE/Spiro OMeTAD/Ni to examine the performance of the OSC. They studied the effect of the temperature of the device within a range of 300–400 K. Anass et al. performed a one-dimensional numerical simulation of a n-i-p OSC with a structure consisting of ITO/PEDOT: PSS/[(Cbz-Mth)-BT]2-PCBM/C61/Al to examine the performance of the OSC, and they studied the influence of variation in the thickness of the active layer, temperature, and the density of the effective states of the electrons and holes in the conduction and valence bands, respectively on the performance of solar cells based on [(Cbz-Mth)-BT]2-PCBM as the photoactive material. The studies conducted by Anass et al. and Muhammad et al. demonstrated an enhancement in thermal stability when compared to previous research. Furthermore, in addition to its thermal stability, our structure achieved a much higher PCE than those constructed by Anass et al. and Muhammad et al. Our structures can maintain high thermal stability at high PCE conditions, representing a notable advancement in OSCs. Our structures can maintain high thermal stability at high PCE conditions of ~20%.

#### 4. Conclusions

Our research demonstrated that the efficiency of inverted ternary OSCs incorporating SnO<sub>2</sub>, C<sub>60</sub>, and PC<sub>60</sub>BM is robust to temperature increases, sustaining less than 10% efficiency loss at 66.76 °C compared to their baseline efficiency at 26.76 °C. This finding underscores the commendable thermal stability of these structures. In addition, we achieved such thermal stability at a high PCE condition, indicating the superb environmental adaptability of investigated structures. However, the configuration using PC<sub>60</sub>BM as the electron transport layer exhibited a relatively lower PCE, highlighting potential areas for improvement. Future studies should expand on these preliminary findings with comprehensive evaluations focusing on the effects of operational temperature on newly synthesized organic semiconductor materials to discover more stable structures and further increase the thermal stability of the organic solar cells. This includes investigating charge mobilities, optimizing cooling systems, assessing material quality, and testing endurance under varying ambient temperatures. From the beginning of the work, we stated that this work involves a simulation of a one-dimensional optoelectronic model. The simulation is limited to a one-dimensional scale and provides findings based on specific parameters related to material properties, standard ambient conditions, defined structure, and a complete standard selection. In addition, practical models or models based on three dimensions have extra challenges and variables due to differences in dimensions compared to the real model, difficulties in controlling ambient conditions, and defects in morphology, deposition method, and material quality, which probably further affect the results.

**Author Contributions:** M.E.A.B.: conceptualization, methodology, writing—original draft preparation, formal analysis, investigation, and data curation; C.Z.: formal analysis, investigation, project administration, resources, funding acquisition, and supervision. All authors have read and agreed to the published version of the manuscript.

**Funding:** This work was supported by the National Natural Science Foundation of China (No. 51976157) and the Fundamental Research Funds for the Central Universities (No. xzy012020075).

**Data Availability Statement:** Data are available from the corresponding author upon reasonable request.

**Conflicts of Interest:** The authors declare no conflicts of interest.

## Nomenclature

Symbol	Description	Unit
$q$	Electrical charge	C
$n$	Concentration of free electrons	$\text{m}^{-3}$
$n_0$	Equilibrium density of electron	$\text{m}^{-3}$
$N_{c,v}$	Effective density of states in the conduction band	$\text{m}^{-3}$
$p_0$	Equilibrium density of holes	$\text{m}^{-3}$
$P$	Concentration of free holes	$\text{m}^{-3}$
$J_{n,p}$	Current density of electrons and holes	$\text{Am}^{-2}$
$v_{th}$	Thermal emission velocity of the carriers	$\text{ms}^{-1}$
$E_{c,v}$	Conduction and valence band	eV
$E_{F,h,e}$	Energy-corresponding Fermi level	eV
$F_{n,p}$	Fermi level in the conduction and valence band	eV
$D_{n,p}$	Diffusion coefficient of electrons and holes	$\text{m}^2 \text{s}^{-1}$
$R_n$	Recombination rate of electrons	$\text{s}^{-1}$
$R_p$	Recombination rate of holes	$\text{s}^{-1}$
$G$	Carrier generation rate	$\text{s}^{-1}$
$K_B$	Boltzmann constant	$\text{JK}^{-1}$
$k$	Rate constant of the reaction	
$T$	Temperature	K
Greek Symbols		
$\epsilon_0$	Permittivity of free space	$\text{Fm}^{-1}$
$\epsilon_r$	Relative permittivity	$\text{Fm}^{-1}$
$\varphi$	Voltage profile	V
$\mu_{e,h}$	Electron and hole mobility	$\text{m}^2 \text{V}^{-1} \text{s}^{-1}$
$\Delta E$	Energy offset	%
$\omega$	Angular frequency of the wave	$\text{rad s}^{-1}$
$\lambda$	Wavelength	nm
Superscripts		
$D$	Electron donor	
$A$	Electron acceptor	

## References

- Coyle, E.D.; Simmons, R.A. (Eds.) Introduction. In *Understanding the Global Energy Crisis*; Purdue University Press: West Lafayette, IN, USA, 2014; pp. 1–8. Available online: <http://www.jstor.org/stable/j.ctt6wq56p.5> (accessed on 15 November 2023).
- Melin, H. Towards a solution to the energy crisis. *Nat. Astron.* **2020**, *4*, 837–838. [CrossRef]
- Mhlanga, D.; Ndhlovu, E. The Implications of the Russia–Ukraine War on Sustainable Development Goals in Africa. *Fudan J. Humanit. Soc. Sci.* **2023**, *16*, 435–454. [CrossRef]
- Borowski, P.F. Mitigating Climate Change and the Development of Green Energy versus a Return to Fossil Fuels due to the Energy Crisis in 2022. *Energies* **2022**, *15*, 9289. [CrossRef]
- Burney, J.A. The downstream air pollution impacts of the transition from coal to natural gas in the United States. *Nat. Sustain.* **2020**, *3*, 152–160. [CrossRef]
- Guan, Y.; Yan, J.; Shan, Y.; Zhou, Y.; Hang, Y.; Li, R.; Liu, Y.; Liu, B.; Nie, Q.; Bruckner, B.; et al. Burden of the global energy price crisis on households. *Nat. Energy* **2023**, *8*, 304–316. [CrossRef]
- Creutzig, F. Fuel crisis: Slash demand in three sectors to protect economies and climate. *Nature* **2022**, *606*, 460–462. [CrossRef]
- Parag, Y.; Fawcett, T.; Hampton, S.; Eyre, N. Energy saving in a hurry: A research agenda and guidelines to study European responses to the 2022–2023 energy crisis. *Energy Res. Soc. Sci.* **2023**, *97*, 102999. [CrossRef]
- The politics of energy security. *Nat. Energy* **2023**, *8*, 1047. [CrossRef]

10. Frilingou, N.; Xexakis, G.; Koasidis, K.; Nikas, A.; Campagnolo, L.; Delpiazzo, E.; Chiodi, A.; Gargiulo, M.; McWilliams, B.; Koutsellis, T.; et al. Navigating through an energy crisis: Challenges and progress towards electricity decarbonisation, reliability, and affordability in Italy. *Energy Res. Soc. Sci.* **2023**, *96*, 102934. [[CrossRef](#)]
11. Ingram, T.; Wieczorek-Kosmala, M.; Hlaváček, K. Organizational Resilience as a Response to the Energy Crisis: Systematic Literature Review. *Energies* **2023**, *16*, 702. [[CrossRef](#)]
12. Hunt, J.D.; Stilpen, D.; de Freitas, M.A.V. A review of the causes, impacts and solutions for electricity supply crises in Brazil. *Renew. Sustain. Energy Rev.* **2018**, *88*, 208–222. [[CrossRef](#)]
13. Wuebbles, D.J.; Fahey, D.W.; Hibbard, K.A. *Climate Science Special Report: Fourth National Climate Assessment, Volume I*; U.S. Global Change Research Program: Washington, DC, USA, 2017. [[CrossRef](#)]
14. Klingelhöfer, D.; Müller, R.; Braun, M.; Brüggmann, D.; Groneberg, D.A. Climate change: Does international research fulfill global demands and necessities? *Environ. Sci. Eur.* **2020**, *32*, 137. [[CrossRef](#)] [[PubMed](#)]
15. Welsby, D.; Price, J.; Pye, S.; Ekins, P. Unextractable fossil fuels in a 1.5 °C world. *Nature* **2021**, *597*, 230–234. [[CrossRef](#)]
16. Kroeger, C. Heat is associated with short-term increases in household food insecurity in 150 countries and this is mediated by income. *Nat. Hum. Behav.* **2023**, *7*, 1777–1786. [[CrossRef](#)] [[PubMed](#)]
17. Guivarch, C.; Le Gallic, T.; Bauer, N.; Fragkos, P.; Huppmann, D.; Jaxa-Rozen, M.; Keppo, I.; Kriegler, E.; Krisztin, T.; Marangoni, G.; et al. Using large ensembles of climate change mitigation scenarios for robust insights. *Nat. Clim. Chang.* **2022**, *12*, 428–435. [[CrossRef](#)]
18. Achakulwisut, P.; Erickson, P.; Guivarch, C.; Schaeffer, R.; Brutschin, E.; Pye, S. Global fossil fuel reduction pathways under different climate mitigation strategies and ambitions. *Nat. Commun.* **2023**, *14*, 5425. [[CrossRef](#)] [[PubMed](#)]
19. Kemfert, C.; Präger, F.; Braunger, I.; Hoffart, F.M.; Brauers, H. The expansion of natural gas infrastructure puts energy transitions at risk. *Nat. Energy* **2022**, *7*, 582–587. [[CrossRef](#)]
20. Masson, V.; Bonhomme, M.; Salagnac, J.-L.; Briottet, X.; Lemonsu, A. Solar panels reduce both global warming and urban heat island. *Front. Environ. Sci.* **2014**, *2*, 14. [[CrossRef](#)]
21. Dunne, N.A.; Liu, P.; Elbarghthi, A.F.A.; Yang, Y.; Dvorak, V.; Wen, C. Performance evaluation of a solar photovoltaic-thermal (PV/T) air collector system. *Energy Convers. Manag.* **2023**, *20*, 100466. [[CrossRef](#)]
22. Nijse, F.J.M.M.; Mercure, J.F.; Ameli, N.; Larosa, F.; Kothari, S.; Rickman, J.; Vercoulen, P.; Pollitt, H. The momentum of the solar energy transition. *Nat. Commun.* **2023**, *14*, 6542. [[CrossRef](#)] [[PubMed](#)]
23. Kalyani, N.T.; Dhoble, S.J. Chapter 10—Empowering the Future With Organic Solar Cell Devices. In *Nanomaterials for Green Energy*; Bhanvase, B.A., Pawade, V.B., Dhoble, S.J., Sonawane, S.H., Ashokkumar, M., Eds.; Micro and Nano Technologies; Elsevier: Amsterdam, The Netherlands, 2018; pp. 325–350. [[CrossRef](#)]
24. Chen, L.X. Organic Solar Cells: Recent Progress and Challenges. *ACS Energy Lett.* **2019**, *4*, 2537–2539. [[CrossRef](#)]
25. Lee, D.; Kim, J.; Park, G.; Bae, H.W.; An, M.; Kim, J.Y. Enhanced Operating Temperature Stability of Organic Solar Cells with Metal Oxide Hole Extraction Layer. *Polymers* **2020**, *12*, 992. [[CrossRef](#)]
26. Cheng, P.; Zhan, X. Stability of organic solar cells: Challenges and strategies. *Chem. Soc. Rev.* **2016**, *45*, 2544–2582. [[CrossRef](#)]
27. Duan, L.; Uddin, A. Progress in Stability of Organic Solar Cells. *Adv. Sci.* **2020**, *7*, 1903259. [[CrossRef](#)] [[PubMed](#)]
28. Yang, W.; Wang, W.; Wang, Y.; Sun, R.; Guo, J.; Li, H.; Shi, M.; Guo, J.; Wu, Y.; Wang, T.; et al. Balancing the efficiency, stability, and cost potential for organic solar cells via a new figure of merit. *Joule* **2021**, *5*, 1209–1230. [[CrossRef](#)]
29. Zhang, C.; Ming, S.; Wu, H.; Wang, X.; Huang, H.; Xue, W.; Xu, X.; Tang, Z.; Ma, W.; Bo, Z. High-efficiency ternary nonfullerene organic solar cells with record long-term thermal stability. *J. Mater. Chem. A* **2020**, *8*, 22907–22917. [[CrossRef](#)]
30. Xu, X.; Fukuda, K.; Karki, A.; Park, S.; Kimura, H.; Jinno, H.; Watanabe, N.; Yamamoto, S.; Shimomura, S.; Kitazawa, D.; et al. Thermally stable, highly efficient, ultraflexible organic photovoltaics. *Proc. Natl. Acad. Sci. USA* **2018**, *115*, 4589–4594. [[CrossRef](#)] [[PubMed](#)]
31. Wang, X.; Feng, J.; Zhang, Z.; Xing, J.; Li, W.; Cui, Y.; Wu, Z.; Yu, W.; Chen, L. Gelation of Electron Transport Layer to Improve the Thermal Stability of Efficient Perovskite Solar Cells. *J. Mater. Chem. C Mater.* **2024**, *12*, 14433–14444. [[CrossRef](#)]
32. Mbilo, M.; Haris, M.; Ryu, D.H.; Mwabora, J.M.; Musembi, R.J.; Lee, S.; Song, C.E.; Shin, W.S. Improved Light Soaking and Thermal Stability of Organic Solar Cells by Robust Interfacial Modification. *Adv. Energy Sustain. Res.* **2024**, *5*, 2300210. [[CrossRef](#)]
33. Di Mario, L.; Garcia Romero, D.; Wang, H.; Tekelenburg, E.K.; Meems, S.; Zaharia, T.; Portale, G.; Loi, M.A. Outstanding Fill Factor in Inverted Organic Solar Cells with SnO<sub>2</sub> by Atomic Layer Deposition. *Adv. Mater.* **2024**, *36*, 2301404. [[CrossRef](#)]
34. Proctor, C.M.; Kuik, M.; Nguyen, T.Q. Charge carrier recombination in organic solar cells. *Prog. Polym. Sci.* **2013**, *38*, 1941–1960. [[CrossRef](#)]
35. Xu, W.; Yi, C.; Yao, X.; Jiang, L.; Gong, X.; Cao, Y. Efficient Organic Solar Cells with Polymer-Small Molecule: Fullerene Ternary Active Layers. *ACS Omega* **2017**, *2*, 1786–1794. [[CrossRef](#)] [[PubMed](#)]
36. Golubev, T.; Liu, D.; Lunt, R.; Duxbury, P. Understanding the impact of C60 at the interface of perovskite solar cells via drift-diffusion modeling. *AIP Adv.* **2019**, *9*, 35026. [[CrossRef](#)]
37. El Karkri, A.; El Malki, Z.; Bouachrine, M.; Serein-Spirau, F.; Sotiropoulos, J.-M. Characterization and simulation study of organic solar cells based on donor–acceptor (D– $\pi$ –A) molecular materials. *RSC Adv.* **2020**, *10*, 18816–18823. [[CrossRef](#)]

38. Khan, M.R.; Jarzabek, B. Optimization and Efficiency Enhancement of Modified Polymer Solar Cells. *preprints* **2023**. [[CrossRef](#)]
39. Anrango-Camacho, C.; Pavón-Ipiales, K.; Frontana-Uribe, B.A.; Palma-Cando, A. Recent Advances in Hole-Transporting Layers for Organic Solar Cells. *Nanomaterials* **2022**, *12*, 443. [[CrossRef](#)]
40. Tang, H.; Bai, Y.; Zhao, H.; Qin, X.; Hu, Z.; Zhou, C.; Huang, F.; Cao, Y. Interface Engineering for Highly Efficient Organic Solar Cells. *Adv. Mater.* **2024**, *36*, 2212236. [[CrossRef](#)]
41. Niederhausen, J.; Mazzi, K.A.; MacQueen, R.W. Inorganicorganic interfaces in hybrid solar cells. *Electron. Struct.* **2021**, *3*, 33002. [[CrossRef](#)]
42. Kong, T.; Wang, R.; Zheng, D.; Yu, J. Modification of the SnO<sub>2</sub> Electron Transporting Layer by Using Perylene Diimide Derivative for Efficient Organic Solar Cells. *Front. Chem.* **2021**, *9*, 703561. [[CrossRef](#)]
43. Eliwi, A.A.; Byranvand, M.M.; Fassel, P.; Khan, M.R.; Hossain, I.M.; Frericks, M.; Ternes, S.; Abzieher, T.; Schwenzer, J.A.; Mayer, T.; et al. Optimization of SnO<sub>2</sub> electron transport layer for efficient planar perovskite solar cells with very low hysteresis. *Mater. Adv.* **2022**, *3*, 456–466. [[CrossRef](#)]
44. Zhu, L.; Zhang, M.; Xu, J.; Li, C.; Yan, J.; Zhou, G.; Zhong, W.; Hao, T.; Song, J.; Xue, X.; et al. Single-junction organic solar cells with over 19% efficiency enabled by a refined double-fibril network morphology. *Nat. Mater.* **2022**, *21*, 656–663. [[CrossRef](#)]
45. Manual: OghmaNano—Organic and Hybrid Material Nano Simulation Tool. Available online: <https://www.oghma-nano.com/docs.html?page=Manual> (accessed on 6 December 2023).
46. MacKenzie, R.C.I.; Shuttle, C.G.; Dibb, G.F.; Treat, N.; von Hauff, E.; Robb, M.J.; Hawker, C.J.; Chabiny, M.L.; Nelson, J. Interpreting the Density of States Extracted from Organic Solar Cells Using Transient Photocurrent Measurements. *J. Phys. Chem. C* **2013**, *117*, 12407–12414. [[CrossRef](#)]
47. Deschler, F.; Riedel, D.; Ecker, B.; von Hauff, E.; Da Como, E.; MacKenzie, R.C.I. Increasing organic solar cell efficiency with polymer interlayers. *Phys. Chem. Chem. Phys.* **2013**, *15*, 764–769. [[CrossRef](#)] [[PubMed](#)]
48. MacKenzie, R.C.I.; Shuttle, C.G.; Chabiny, M.L.; Nelson, J. Extracting Microscopic Device Parameters from Transient Photocurrent Measurements of P3HT:PCBM Solar Cells. *Adv. Energy Mater.* **2012**, *2*, 662–669. [[CrossRef](#)]
49. Farooq, W.; Khan, A.D.; Khan, A.D.; Noman, M. Enhancing the power conversion efficiency of organic solar cells. *Optik* **2020**, *208*, 164093. [[CrossRef](#)]

**Disclaimer/Publisher’s Note:** The statements, opinions and data contained in all publications are solely those of the individual author(s) and contributor(s) and not of MDPI and/or the editor(s). MDPI and/or the editor(s) disclaim responsibility for any injury to people or property resulting from any ideas, methods, instructions or products referred to in the content.